ACS APPLIED MATERIALS & INTERFACES

Research Article

www.acsami.org

Template-Free Synthesis of Amorphous Double-Shelled Zinc–Cobalt Citrate Hollow Microspheres and Their Transformation to Crystalline $ZnCo_2O_4$ Microspheres

Qingshui Xie,[†] Feng Li,[‡] Huizhang Guo,[†] Laisen Wang,[†] Yuanzhi Chen,[†] Guanghui Yue,[†] and Dong-Liang Peng*[,†]

[†]Department of Materials Science and Engineering, College of Materials, Xiamen University, Xiamen 361005, China

[‡]Department of Materials Science and Engineering, Zhejiang University, Hangzhou 310027, China

Supporting Information

ABSTRACT: A novel and facile approach was developed for the fabrication of amorphous double-shelled zinc–cobalt citrate hollow microspheres and crystalline double-shelled $ZnCo_2O_4$ hollow microspheres. In this approach, amorphous double-shelled zinc–cobalt citrate hollow microspheres were prepared through a simple route and with an aging process at 70 °C. The combining inward and outward Ostwald ripening processes are adopted to account for the formation of these double-shelled architectures. The double-shelled $ZnCo_2O_4$ hollow microspheres can be prepared via the perfect morphology inheritance of the double-shelled zinc–cobalt citrate hollow microspheres, by calcination at 500 °C for 2 h. The resultant double-shelled $ZnCo_2O_4$ hollow microspheres manifest a large reversible capacity, superior cycling stability, and good rate capability.

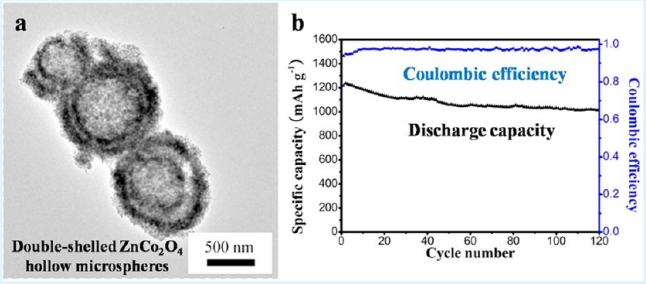

KEYWORDS: *zinc–cobalt citrate, Ostwald ripening, double-shelled hollow microspheres, $ZnCo_2O_4$, anode*

INTRODUCTION

In the last decades, lithium-ion batteries (LIBs) have become increasingly important power sources for use in portable electronic and high energy areas including electric vehicles and hybrid electric vehicles.[1,2] A commercial lithium-ion battery today uses graphite as the anode material. However, graphite-based lithium-ion batteries have some obvious disadvantages, including relatively poor cyclability and low theoretical capacity (372 mA h g^{-1}). Therefore, tremendous efforts have been carried out to exploit various advanced anode materials.[3] Recently, various metals and metal oxides that undergo alloying/dealloying and/or conversion reactions have been extensively studied as anodes for LIBs. For example, various tin oxides including binary and ternary systems have acquired extensive concern because of their high capacity (993 mA h g^{-1}) based on alloying/dealloying reaction mechanism.[4,5] However, the large capacity fading, volume variation during discharge–charge cycling and the irreversible capacity loss (ICL) at the first cycle limit their practical applications. It has been well demonstrated that these problems could be moderately alleviated by various approaches, including (1) incorporating appropriate matrix elements, (2) restricting the voltage range of cycling vs Li, and (3) reducing the particle size to nanosize.[6−12] Among these approaches, that addition of one or more matrix elements in the electrode material is one of the most common strategies. Matrix elements that may not be electrochemically active will function as a matrix and help in suppressing the capacity fading, buffering the strain due to large volume variations arose from the repeated Li^+ insertion/extraction and reducing the irreversible capacity loss (ICL).

Recently, transition metal oxides, such as TiO_2, Fe_3O_4, MoO_2, and Co_3O_4, have been intensely exploited as the anodes for LIBs.[13−19] Of all the oxides studied so far, Co_3O_4 has been regarded as one of the most promising electrode candidates because of its large capacity and good cyclability. Therefore, many methods have been developed to fabricate various morphologies of Co_3O_4 and improve their electrochemical properties.[20−22] For example, porous Co_3O_4 nanocapsules were successfully produced via a solvothermal route and subsequent calcination process.[23] Also, Co_3O_4 nanoparticles were prepared by the molten salt method.[24] Both of them exhibited excellent electrochemical performances when the electrochemical measurements were proceeded. However, the disadvantages of Co_3O_4 are also obvious, such as the toxicity and high cost of cobalt. Additionally, the large voltage hysteresis which may lead to huge round-trip inefficiencies (poor energy efficiency of the electrodes) in Co_3O_4 are undoubtedly the most serious drawback for their practical applications.[3,24−27] Therefore, various efforts have been made to partially replace Co in Co_3O_4 by cheaper and more eco-friendly alternative metals,

Received: February 24, 2013
Accepted: May 29, 2013
Published: May 29, 2013

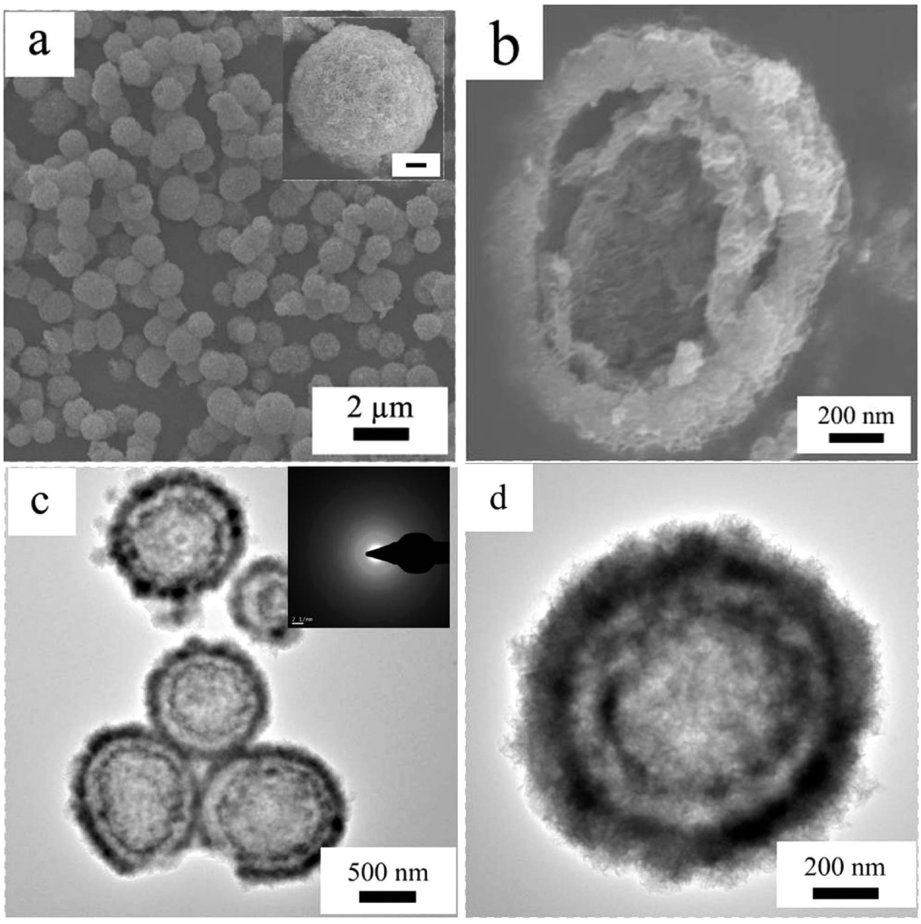

Figure 1. (a) SEM micrograph of the double-shelled zinc−cobalt citrate hollow microspheres. The inset exhibits a magnified micrograph of an individual microsphere. (b) SEM image of a broken microsphere. (c) Low-magnification TEM micrograph of the double-shelled zinc−cobalt citrate hollow architectures. The inset is the corresponding SAED pattern. (d) High-magnification TEM micrograph of an individual microsphere.

such as Ni, Cu, Zn, Fe, and Mn, which do not sacrifice its electrochemical performance.[7,28−34] Considering that Zn^{2+} replaces Co^{2+} at the tetrahedral site in Co_3O_4, spinel $ZnCo_2O_4$ is isomorphic to the Co_3O_4 crystal structure. Both zinc and cobalt which are electrochemically active to lithium could contribute to lithium storage in a complementary manner.[14] As a result, ternary $ZnCo_2O_4$ has been considered as an attractive anode for LIBs.[13,35] Therefore, many methods have been developed to fabricate $ZnCo_2O_4$, such as the molten salt method, hydrothermal method, urea combustion method and electrospinning method.[7,36−38] Among them, the molten salt method (MSM) is one of the simplest and the most low-cost methods frequently used to synthesize various simple and complex oxides.[39−43] It is well-known that the preparation method, the morphology of the electrode materials and the phase purity have a crucial effect on electrochemical properties.[25,33] As a unique class of structure materials, hollow structures have been widely investigated for LIBs due to their special and unique structures.[44] However, for $ZnCo_2O_4$, its double-shelled hollow architecture applied as anode for LIBs has not been reported so far.

In this article, a novel and facile approach to fabricate amorphous double-shelled zinc−cobalt citrate hollow microspheres and crystalline double-shelled $ZnCo_2O_4$ hollow microspheres is reported. The combining inward and outward Ostwald ripening mechanism is applied to interpret the evolution process of double-shelled zinc−cobalt citrate hollow microspheres. By calcination of the as-obtained zinc−cobalt citrate composite at 500 °C for 2 h, the double-shelled $ZnCo_2O_4$ hollow microspheres were produced via perfect morphology inheritance. To the best of our knowledge, this is the first successful synthesis of the double-shelled $ZnCo_2O_4$ hollow microspheres. The exploration of the electrochemical performance show that the as-prepared double-shelled $ZnCo_2O_4$ hollow microspheres manifest a large reversible capacity, good rate capability, and superior cycling stability.

EXPERIMENTAL SECTION

2.1. Synthesis. In a typical procedure, amorphous zinc citrate solid microspheres were first synthesized through a simple one-step route under mild conditions as described in our earlier literature.[22] Newly prepared zinc citrate solid microspheres (0.04 g) were added to a certain concentration of cobalt nitrate solution (20 mL) followed by ultrasonic treatment for 15 min. Afterward, the resulting mixtures were aged for 6 h at 70 °C. The resultant composite was harvested by centrifugation and rinsed with distilled water for several times and then dried at 80 °C for 10 h. Finally, the double-shelled $ZnCo_2O_4$ hollow microspheres were obtained by the calcination of zinc−cobalt citrate composite at 500 °C for 2 h in air.

2.2. Characterization. X-ray diffraction (XRD) measurements were recorded with a PANalytical X′ pert PRO X-ray diffractometer using Cu Kα radiation (40 kV, 60 mA). Scanning electron microscopy (SEM) micrographs were obtained using a LEO-1530 field-emission scanning electron microscope equipped with an energy dispersive X-ray spectrometer (EDS). Transmission electron microscopy (TEM) observations were performed on a JEM-2100 electron microscope

dx.doi.org/10.1021/am400696x | ACS Appl. Mater. Interfaces 2013, 5, 5508−5517

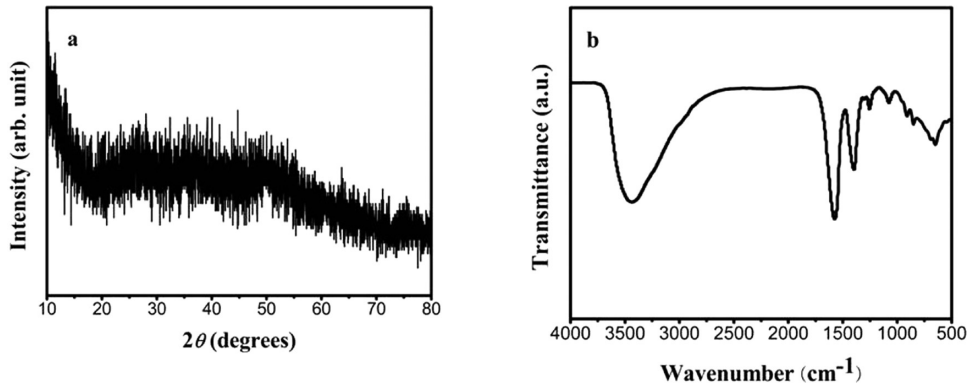

Figure 2. (a) XRD pattern and (b) FT-IR spectrum of the double-shelled zinc–cobalt citrate hollow microspheres.

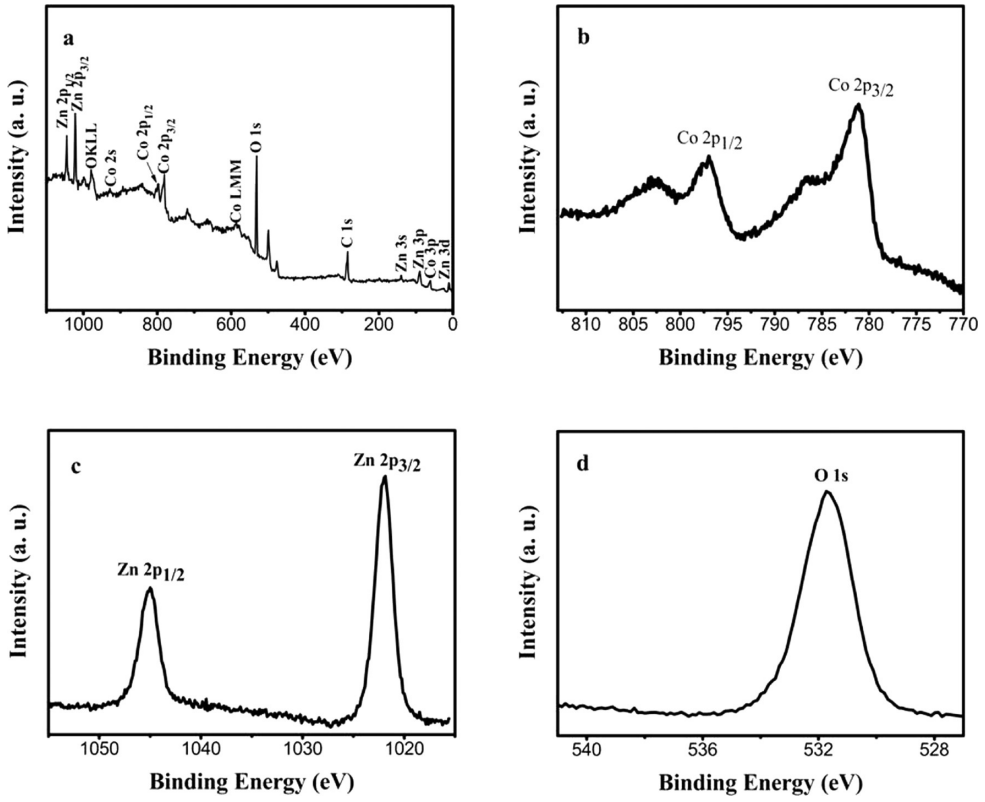

Figure 3. XPS spectra of the double-shelled zinc–cobalt citrate hollow microspheres: (a) full spectrum and high-resolution (b) Co 2p, (c) Zn 2p, (d) O 1s spectra.

operating at 200 kV. The thermogravimetric and differential thermal analyses (TG-DTA) were performed on a Du Pont Instrument 1090B thermal analyzer. Fourier-transform infrared (FTIR) spectra were carried out on a Nicolet Nexus-670 FT-IR spectrometer. X-ray photoelectron spectra (XPS) were acquired from the PHI QUANTUM 2000. The Brunauer–Emmett–Teller (BET) surface area and pore volume were tested using a TriStar 3020 system.

2.3. Electrochemical Measurements. Electrochemical properties were measured using two-electrode cells assembled in an argon-filled glovebox. The working electrode consists of 75 wt % active materials (that is double-shelled $ZnCo_2O_4$ hollow microspheres), 15 wt % carbon black, and 10 wt % poly (vinyl difluoride) (PVDF) using N-methyl pyrrolidone (NMP) as solvent. The mixed suspension was coated on to a nickel gauze current collector and then dried at 70 °C for 12 h. The nickel gauze was then pressed into circular plates (16 mm diameter) to ensure better electrical contact between electrode material and Ni-substrate. The mass of $ZnCo_2O_4$ in the electrode ranges from 3 to 4 mg, and the effective electrode area is 0.33 cm^2. The electrolyte solution was 1 M $LiPF_6$ dissolved in equal volume of ethylene carbonate and diethyl carbonate mixed solution. Lithium metal was adopted as the counter-electrode. The galvanostatic cycling was performed on a multichannel battery testing system (Land, China) and cyclic voltammetry (CV) was measured on a PARSTAT 2273 potentiostat at 0.1 mV s^{-1}. The active material were took out in the disassembled cells for ex situ XRD and TEM observations as described in the literature.[13]

■ RESULTS AND DISCUSSION

Zinc–cobalt citrate composite obtained from the resulting suspension and aged at 70 °C for 6 h were employed as the precursor for the fabrication of double-shelled $ZnCo_2O_4$ hollow microspheres. Figure 1 presents the SEM and TEM images of the precursor. The precursor is composed of dispersed microspheres with a diameter of about 1.3 μm (Figure 1a). The high-magnification SEM micrograph (inset of Figure 1a)

shows that the surface of the microspheres is quite rough and loose. Figure 1b demonstrates a broken microsphere. Two shells and the inner hollow space can be clearly observed. Figure 1c and 1d further confirm the interior hollow void and double-shelled structure of the precursor. The thickness of the outer and inner shell is about 180 and 90 nm, respectively. The selected-area electron diffraction (SAED) pattern (inset of Figure 1c) and the powder XRD pattern (Figure 2a) confirm that the zinc−cobalt citrate microspheres are amorphous. EDS microanalysis of the precursor shows a Zn/Co ratio of about 0.5 (see Figure S1a in the Supporting Information). The as-prepared precursor is further characterized by FT-IR spectroscopy. As depicted in Figure 2b, the IR spectrum displays two intense absorption bands at 1573 and 1398 cm^{-1}, which can be attributed to the antisymmetric and symmetric stretching vibrations for the carboxylate groups of the coordinated citrates, respectively. Compared to free citric acid, both of the bands shift to lower frequencies, suggesting complexation to metal ion.[45−48] The typical absorption bands between 1700 and 1710 cm^{-1} arising from undissociated carboxylic acid groups could not be observed, which demonstrates that each carboxylic acid group is deprotonated.[48−50] The strong peaks at 3435 cm^{-1} can be assigned to the vibrations of −OH groups for absorbed water. The typical survey XPS spectrum of the precursor is depicted in Figure 3a, which shows the presence of Zn, Co, O, and C elements. Figure 3b shows the high-resolution Co 2p spectrum. Two peaks at 781.0 eV for Co $2p_{3/2}$ and 796.9 eV for Co $2p_{1/2}$ are observed. The peaks at 786.8 and 802.7 eV can be ascribed to the satellite peaks, indicating the Co (II) oxidation state of precursor. The results are in good agreement with the literature.[51,52] Figure 3c reveals the high-resolution Zn 2p spectrum. Two peaks located at 1045.0 and 1021.9 eV are assigned to Zn $2p_{3/2}$ and Zn $2p_{1/2}$ of Zn(II), respectively. The O 1s peak at 531.9 eV correspond to the oxygen species in precursor in Figure 3d. From the above analysis, the as-obtained precursor can be deduced to be zinc−cobalt(II) citrate composite.

To further understand the formation mechanism of double-shelled zinc−cobalt citrate hollow architectures, we acquired and characterized samples with different aging times. Without aging at 70 °C, the initial zinc citrate particles have the morphology of solid microspheres with smooth surface in Figure S2a and S2b (see the Supporting Information). With a short aging time of 2 h after ultrasonication, the yolk−shell microspheres can be seen in Figure S2c, d in the Supporting Information. The high-magnification SEM micrograph (inset of Figure S2c in the Supporting Information) reveals the rather rough and loose surface of the microspheres. EDS microanalysis (see Figure S1b in the Supporting Information) shows a Zn/Co ratio of about 2. As the aging time increases to 4 h, as displayed in Figure S2e, f in the Supporting Information, the solid cores gradually hollow to form double-shelled microspheres. It can be observed that the hollow interior of the core spheres are not completely finished at this stage (Figure S2f in the Supporting Information). EDS microanalysis shows a Zn/Co ratio of about 0.74 (Figure S1c in the Supporting Information). As the aging time further increases to 6 h, the well-defined double-shelled hollow microspheres can be observed (Figure 1). Extending the aging time longer than 6 h, the morphology of the double-shelled hollow structures nearly does not change. Therefore, the evolution of the morphology for the samples with aging time can be reasonably concluded as follows: solid microspheres (0 h)→ yolk-shell microspheres (2 h)→ double-shelled hollow microspheres with the uncompleted hollow interior of the core spheres (4 h)→ the well-defined double-shelled hollow microspheres (6 h).

According to the above experimental observations and analysis, the combining inward and outward Ostwald ripening processes are suggested to interpret the formation process of the double-shelled zinc−cobalt citrate hollow microspheres, which is similar to the previous reported literature.[53−56] This ripening commonly relates to the growth process of particles in the solution. The larger particles grow up at the consumption of smaller ones because of the higher solubility of smaller particles.[21] Inward ripening process refers to the mass reorganization starting from the outmost surfaces; conversely, the outward ripening process involves the mass conversion initiating from the central area of particle aggregate.[53] The surfaces of zinc citrate microspheres are rich in functional groups available for metal ion adsorption, which is similar to the carbonaceous particles reported earlier.[57] When zinc citrate solid microspheres were dispersed into cobalt nitrate solution, cobalt ions would adsorb on the surfaces of zinc citrate solid microspheres, thus replacing part of zinc ions. As a result, the smooth surfaces of zinc citrate solid microspheres became rough and loose (see Figure S2c in the Supporting Information). Then the particles loosely located on the outermost surfaces of the solid microspheres serve as starting redeposition sites and the Ostwald ripening process would first take place at a particular region underneath the immediate surface layer, leading to the formation of a yolk-shell structure. Afterward, the solid core spheres of yolk−shell microspheres ripened outward (Figure S2f in the Supporting Information), which finally formed the double-shelled hollow structures.[53] It is worth noting that more and more zinc ions would be replaced by cobalt ions as the ripening proceeds, which is confirmed by the EDS microanalysis (Figure S1b, c in the Supporting Information). Finally when the double-shelled hollow structures form completely, the molar ratio of zinc and cobalt is approximately equal to 0.5 (see Figure S1a in the Supporting Information).

TG-DTA analysis was performed to further characterize the thermal properties of the double-shelled zinc−cobalt citrate hollow microspheres (Figure 4). A gradual weight loss at temperatures below 287 °C is due to the dehydration of physically adsorbed water. The following weight loss of 44.1% between 280 and 320 °C is attributed to the decomposition of zinc−cobalt citrate to $ZnCo_2O_4$, corresponding to a sharp exothermic peak near 295 °C in the DTA curve. As the

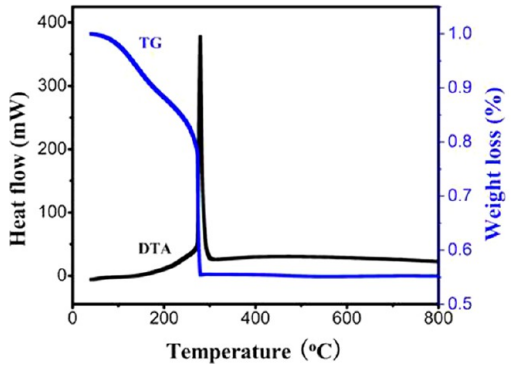

Figure 4. TG-DTA curves for the double-shelled zinc−cobalt citrate hollow microspheres.

temperature further increases, the amorphous double-shelled zinc−cobalt citrate hollow microspheres completely transform into crystalline $ZnCo_2O_4$ microspheres, which is confirmed below by XRD analysis.

Figure 5 demonstrates the XRD pattern of the product obtained using zinc−cobalt citrate as precursor after calcination

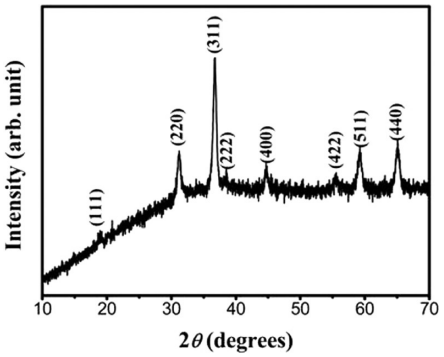

Figure 5. XRD pattern of the double-shelled $ZnCo_2O_4$ hollow microspheres.

at 500 °C for 2 h. All the diffraction peaks can be indexed to cubic $ZnCo_2O_4$ with a spinel structure (JCPDS card no. 23−1390). No additional diffraction peaks from other than $ZnCo_2O_4$ are detectable, implying the high purity of the product. The lattice parameter a is 0.81047 nm. The calculated value is comparable with the literature (a = 0.81267 nm, a = 0.81020 nm, and a = 0.81103 nm).[36] From the XRD pattern, the mean grain size of the primary $ZnCo_2O_4$ particles was calculated to be approximately 16.8 nm using the scherrer equation.

The morphology and the microstructure of the as-obtained $ZnCo_2O_4$ are further characterized by SEM and TEM. As displayed in Figure 6, the product consists of disperse double-shelled hollow microspheres, which demonstrates that the $ZnCo_2O_4$ microstructures have perfectly inherited the morphology of the zinc−cobalt citrate structures after calcination. The average diameter of the double-shelled $ZnCo_2O_4$ hollow microspheres is 0.9 μm, indicating that the microspheres shrink during the transformation from zinc−cobalt citrate to $ZnCo_2O_4$. The SEM micrograph with a high magnification (inset in Figure 6a) reveals that the surface of the $ZnCo_2O_4$ microsphere is made up of many interconnected $ZnCo_2O_4$ nanoparticles with an average size of about 40 nm and numerous nanopores in the outer shell. Figure 6b demonstrates a magnified broken microsphere, the inner shell can be easily discerned, having a similar particle assembly feature and many nanopores as that of the outer shell. The double-shelled structures of the as-produced $ZnCo_2O_4$ microspheres can also be validated by the TEM observation (Figure

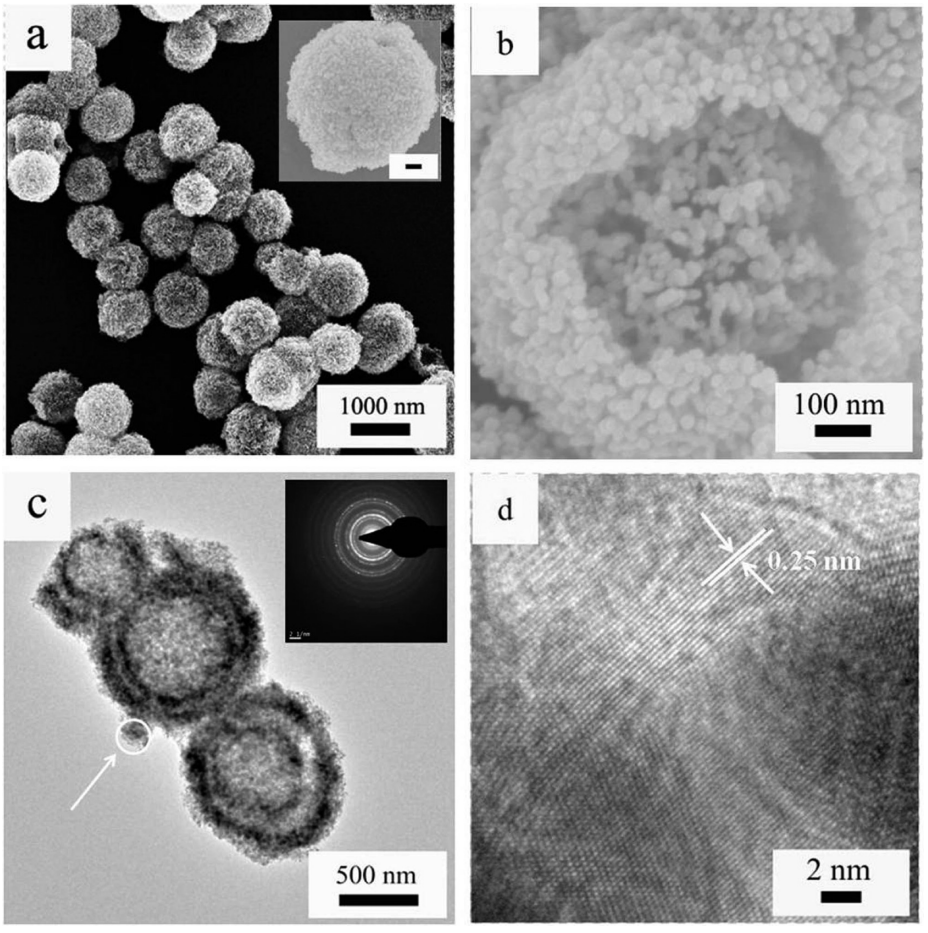

Figure 6. (a) SEM micrograph of double-shelled $ZnCo_2O_4$ hollow microspheres. The inset shows a magnified individual microsphere. (b) The SEM image of a broken microsphere. (c) TEM micrograph of the double-shelled $ZnCo_2O_4$ hollow microspheres. The inset is the corresponding SAED pattern. (d) HRTEM micrograph of the shell area indicated by an arrow and a circle in c.

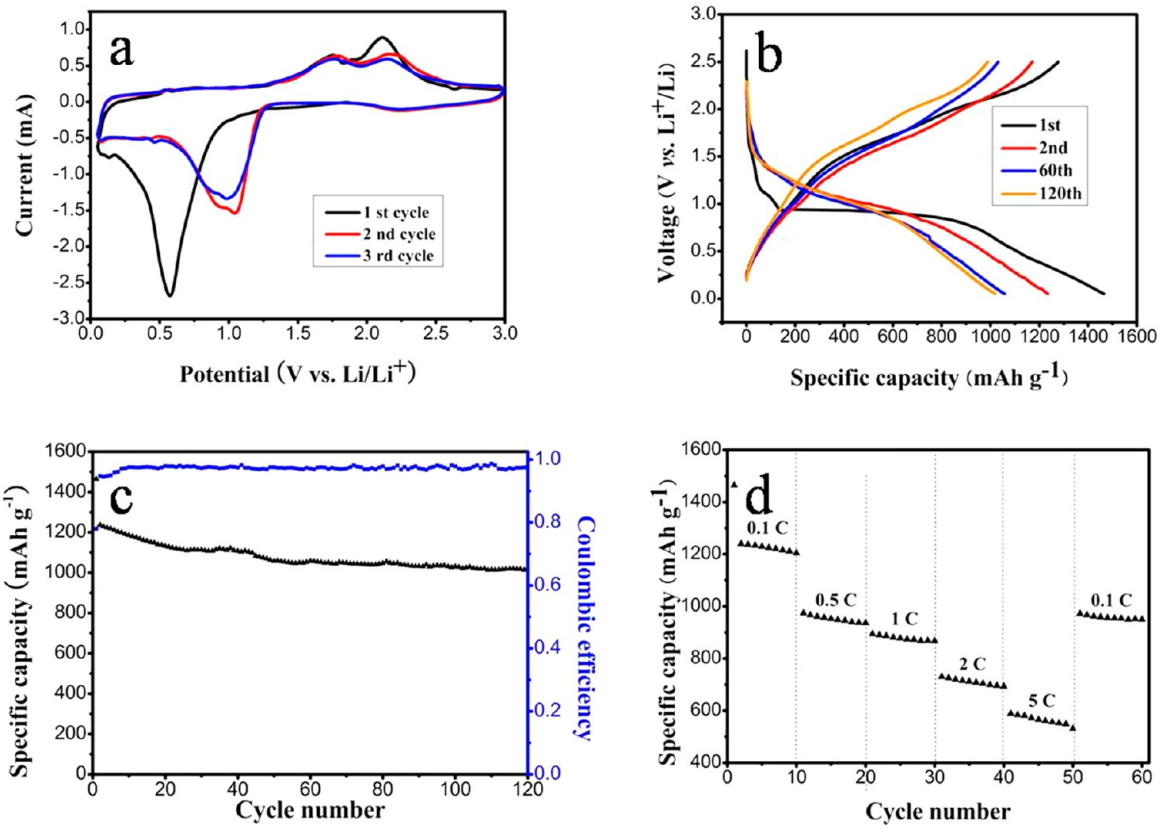

Figure 7. (a) Cyclic voltammograms of the double-shelled $ZnCo_2O_4$ hollow microsphere measured at 0.1 mV s^{-1} in 0.01−3 V. (b) Discharge−charge curves of the double-shelled $ZnCo_2O_4$ hollow microsphere cycled at 90 mA g^{-1} in 0.005−3 V. (c) Specific capacity and Coulombic efficiency vs cycle number of the double-shelled $ZnCo_2O_4$ hollow microspheres at 90 mA g^{-1}. (d) Rate performance of the electrode made from double-shelled $ZnCo_2O_4$ hollow microspheres.

6c). The SAED pattern demonstrates that the double-shelled $ZnCo_2O_4$ hollow microspheres are polycrystalline (inset in Figure 6c). The HRTEM image depicted in Figure 6d exposes clear lattice fringes with a lattice spacing of 0.25 nm, corresponding to the {311} planes of the cubic spinel $ZnCo_2O_4$. The textural feature of $ZnCo_2O_4$ microspheres was further characterized by nitrogen sorption measurement at 77 K (see Figure S3a in the Supporting Information). It can be seen that the Brunauer−Emmett−Teller (BET) surface area of the double-shelled hollow structures is 20.9 m^2 g^{-1}. The pore size distribution spectrum (see Figure S3b in the Supporting Information) was acquired through the Barrett−Joyner−Halenda method, which shows a pore size distribution from 5 to 40 nm in the mesoporous region, centered at 15 nm. Studies revealed that too large surface area would lead to more significant side reactions with electrolyte in LIBs, which makes it have more chance of capacity fading.[24,25,27,36] Compared with the reported values of surface area of the $ZnCo_2O_4$ (BET (nanowires) = 68.86 m^2 g^{-1}, BET (nanotubes) = 21.9 m^2g^{-1} and BET (nanoparticles) = 11.5 m^2 g^{-1}), our BET value is moderate.[36,38,58] Recently, $ZnCo_2O_4$ nanoparticles were fabricated through a simple molten salt method which revealed a good electrochemical performance.[36] Unlike the molten salt method, the $ZnCo_2O_4$ fabricated by our method possess hollow structure and compose of many interconnected $ZnCo_2O_4$ nanoparticles and numerous nanopores in the inner and outer shells. Such a textural feature of $ZnCo_2O_4$ will provide rapid ion transport and good access between the electrolyte and the electrode and alleviate the mechanical strain owing to the volume variations during discharge−charge cycle, which is beneficial to improve their electrochemical properties.

The electrochemical properties of the $ZnCo_2O_4$ are tested by cyclic voltammetry and galvanostatic discharge−charge measurements. Typical cyclic voltammograms (CVs) of the electrode made from the double-shelled $ZnCo_2O_4$ hollow microspheres are displayed in Figure 7a. In the first cathodic sweep, there are two peaks at 0.12 and 0.57 V respectively. The large, broad and irreversible reduction peak located at 0.57 V is attributed to the decomposition of $ZnCo_2O_4$ to Zn and Co.[31] The relatively weak peaks centered at 0.12 V is attributed to the formation of Li−Zn alloy. In the anodic sweep, two main oxidation peaks centered at 1.7 and 2.1 V correspond to the oxidation of Zn to Zn^{2+} and Co to Co^{3+}.[58] A very weak peak at 0.54 V can be carefully discerned, which arises from the dealloying process of Li−Zn alloy. The second discharge sweep distinguishes from the first and comprises a doublet cathodic peak at about 0.94 and 1.04 V, indicating different electrochemical mechanisms. Similar shifts in the anodic/cathodic peaks voltage values were noted both in the CV curses of $ZnCo_2O_4$ and Co_3O_4 nanoparticles prepared by molten salt method.[24,36] Compared with $ZnCo_2O_4$ nanoparticles, the slight differences in the peak values are attributed to the different preparation method. For Co_3O_4, the alloying/dealloying peaks of Li−Zn alloy are absent. The subsequent CV curves superimpose well, implying the excellent stability and cyclability for the $ZnCo_2O_4$ electrode. Representative discharge−charge profiles of the $ZnCo_2O_4$ electrode at 90 mA g^{-1} in the voltage window of 0.005−3 V are revealed in Figure 7b. The initial

dx.doi.org/10.1021/am400696x | ACS Appl. Mater. Interfaces 2013, 5, 5508−5517

capacities for the first discharge and charge are 1464 and 1141 mA h g^{-1}, respectively, corresponding to a Coulombic efficiency of 77.4%. There is a clear potential plateau at about 0.93 V (vs Li^+/Li) in the first discharge curve. Afterward, the voltage decrease gradually to 0.005 V. The plateau region is ascribed to the structure damage or amorphization and the sloping region arise from the solid electrolyte interphase (SEI) formed at the electrode/electrolyte interface and is also partially due to the formation of a polymeric layer on the metal nanoparticles.[28,36,59] According to the literature, the SEI layer contains LiF, Li_2CO_3 and alkylcarbonate lithium salts ($ROCO_2Li$).[59−61] The extra capacity at the first discharge is attributed to the formation of SEI layer and polymeric layer.[9,13,36] In the following cycles, the long discharging plateau becomes steeper and moves upward, consequently forming a long slope between 1.3 and 0.75 V. This phenomenon is in accordance with the results reported in the literature.[13,58] The discharge capacity versus cycle number at 90 mA g^{-1} and the corresponding Coulombic efficiencies are demonstrated in Figure 7c. The $ZnCo_2O_4$ electrode reveals a large capacity fading during the initial 30th cycle. Afterward, the reversible capacities decrease at a slower and slower rate and maintain a nearly constant value above 1025 mA h g^{-1}. Even after 120 cycles, a high discharge capacity of 1019 mA h g^{-1} are still retained, demonstrating the high specific capacity and superior cyclability. Coulombic efficiency after 120th cycle is about 97.8%. Besides the superior specific capacity and excellent cyclability, the rate capability is another important parameter for electrode materials. The rate capability of the $ZnCo_2O_4$ electrode was evaluated at five C rates (0.1, 0.5, 1, 2 and 5*C*, 1*C* = 900 mA h g^{-1}) and the results are displayed in Figure 7d. As the *C* rate gradually increases from 0.1 to 5 C, the average discharge capacity decreases from 1220, 955, 880, 713, and 570 mA h g^{-1}. After the high rate discharge−charge cycles, a high discharge capacity (955 mA h g^{-1}) could be resumed when the rate is performed at 0.1*C* again.

According to previous literature, the electrochemical reactions referred to the discharge and charge processes can be clarified as follows[13,36]

$$ZnCo_2O_4 + 8Li^+ + 8e \rightarrow Zn + 2Co + 4Li_2O \quad (1)$$

$$Zn + Li^+ + e \leftrightarrow LiZn \quad (2)$$

$$Zn + Li_2O \leftrightarrow ZnO + 2Li^+ + 2e \quad (3)$$

$$2Co + 2Li_2O \leftrightarrow 2CoO + 4Li^+ + 4e \quad (4)$$

$$2CoO + 2/3Li_2O \leftrightarrow 2/3Co_3O_4 + 4/3Li^+ + 4/3e \quad (5)$$

Electrochemical impedance spectra (EIS) of the $ZnCo_2O_4$ electrode at different discharge−charge cycles were measured at 3 V, as exhibited in Figure 8. The solution resistances (R_s) and the calculated charge transfer resistances (R_{ct}) of the cells after first and fifth cycles are 4.51, 5.22 Ω and 69.7, 175.5 Ω, respectively. After five cycles, the solution resistance of the cells increases slightly. However, the charge transfer resistance has an obvious increase. The increase in resistance may lead to a capacity fading during the cycling process. The result is consistence with the discharge−charge cyclic performance, which demonstrates a large capacity degradation in the initial 30th cycles. To further clarify the electrochemical mechanism, the ex situ XRD and TEM were performed on the electrode material. As depicted in Figure 9, the diffraction peaks could be

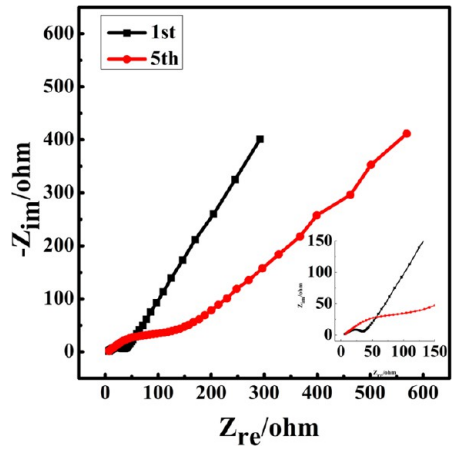

Figure 8. Nyquist plots of the $ZnCo_2O_4$ electrode after first and fifth cycles (the inset is a magnified section).

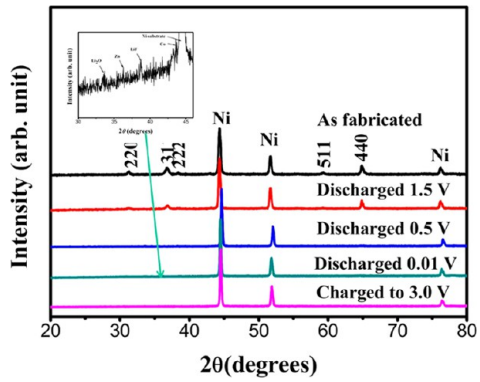

Figure 9. Ex situ XRD patterns of $ZnCo_2O_4$ electrode with various discharge−charge state at the first cycle. The inset shows a magnified XRD pattern.

assigned to cubic $ZnCo_2O_4$ and Ni substrate when the electrode discharged to 1.5 V, which is similar to that of the pristine electrode, suggesting that the electrochemical process would not initiate until 1.5 V. However, only peaks attributed to Ni substrate can be discerned when the electrode discharged to 0.5 V. This phenomenon indicates that the structure damage or amorphization takes place between 1.5 and 0.5 V and is in accordance with the results of galvanostatic discharge−charge profiles with a large voltage plateau located at 0.93 V.[13] When the electrode is further discharged to 0.01 V the peaks corresponding to metallic Zn and Co or Li_2O are covered by the strong Ni peaks. In the magnified XRD pattern ranging from 30 to 46°, some weak peaks at around 33.5, 36.3, 38.7, and 43.6° can be carefully observed, which are attributed to Li_2O (111), Zn (002), LiF (111) and Co (220), respectively (inset of Figure 9). The presence of the LiF diffraction peak may affirm the formation of SEI layer during the discharge process. When the electrode is recharged to 3.0 V, there is no peak with respect to the oxidized electrode species. This may be ascribed to the nanoscale nature of the oxidized electrode species. Moreover, the spinel structure of electrode material is mostly damaged at the first discharge process and could not be regenerated during the subsequent charging process.[13,58] Additionally, the morphology of the active materials after first and 120th cycles are characterized by ex situ TEM. The double-shelled hollow structures are almost maintained after first cycle (Figure 10a). The corresponding SAED pattern is depicted in

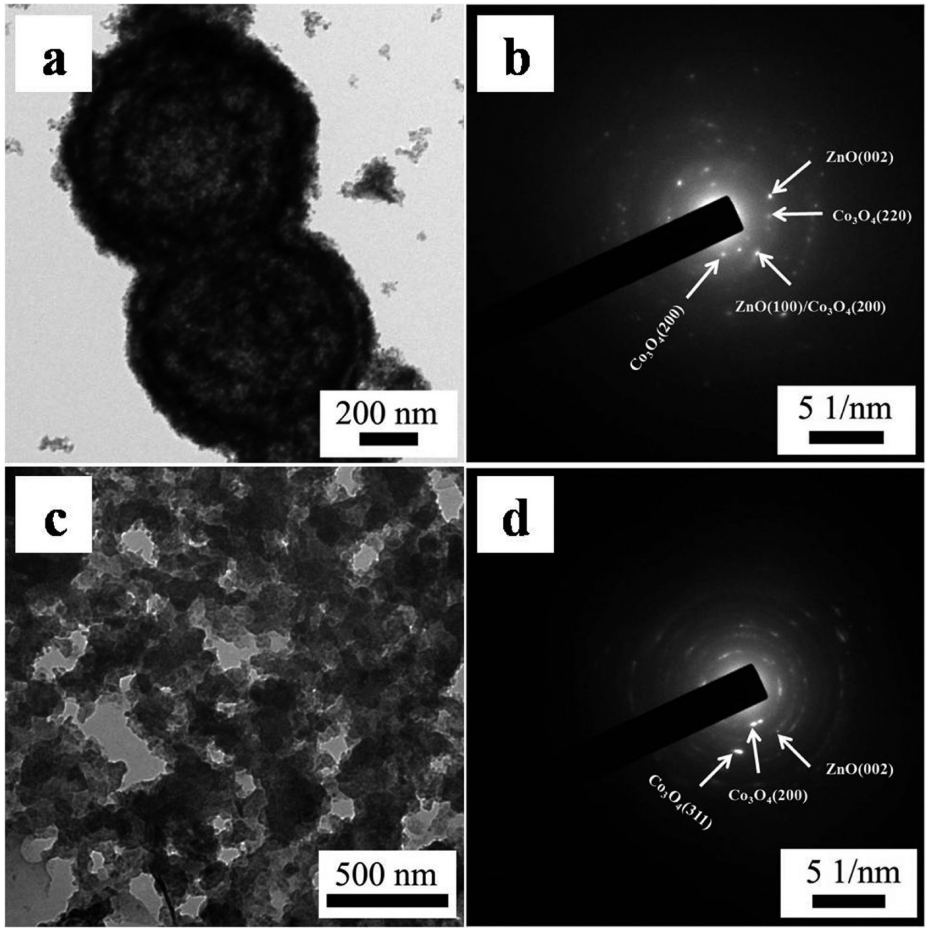

Figure 10. Ex situ TEM micrographs and corresponding SAED patterns of the electrode at 3.0 V after (a, b) the first cycle and (c, d) 120 cycles.

Figure 10b. The superposition of the diffuse spots and the diffuse rings are obviously observed, which implies the presence of crystallites with very small sizes and corroborates the formation of ZnO and Co_3O_4. As shown in Figure 10c, the double-shelled structures are destroyed and cracked into nanoparticles after 120th cycles. However, the SAED pattern is similar with that of the electrode material after first cycle. Combined with the results of EIS, ex-situ XRD and TEM, the reaction mechanism based on the eqs 1−5 is proposed.

On the basis of the above results, the as-fabricated $ZnCo_2O_4$ electrode exhibits high specific capacity, superior cycling stability, and excellent rate performance. To the best of our knowledge, this is the first report on utilizing double-shelled $ZnCo_2O_4$ hollow microspheres as an electrode material for LIBs. The superior electrochemical performances of the as-synthesized $ZnCo_2O_4$ electrode arise from its special structure on the following factors: (1) The nanometer-sized building blocks of the double-shelled $ZnCo_2O_4$ hollow microspheres would provide a short path for Li^+ ion diffusion, leading to excellent rate capability.[62] (2) The porosity and the moderate surface area of the double-shelled structures can provide good channel of the electrolyte to the electrode surface and improve the contact between electrode material and the electrolyte. Additionally, the nanometer-sized building blocks and porosity can effectively buffer the large volume change and alleviate the pulverization problem during the repeated Li^+ insertion/extraction, thus improving the cycling performance.[9,38] (3) Compared to the single-shelled structure, this double-shelled structure is considered to be more robust, because it can tolerate structural degradation more efficiently during cycling process.[17]

CONCLUSIONS

In summary, amorphous double-shelled zinc−cobalt citrate hollow microspheres were successfully prepared through a novel facile route. The combining inward and outward Ostwald ripening processes could be an underlying mechanism for the formation of double-shelled zinc−cobalt citrate hollow microspheres. After the calcination of the zinc−cobalt citrate composite at 500 °C for 2 h, the double-shelled $ZnCo_2O_4$ hollow microspheres are synthesized for the first time. The as-obtained $ZnCo_2O_4$ reveals a large reversible capacity of 1235 mA h g^{-1} at 90 mA g^{-1}, good cycling stability and excellent rate capability. The results of ex situ XRD and TEM investigation are in accordance with the suggested reaction mechanism. Both zinc and cobalt, which are electrochemically active to lithium, could contribute to lithium storage in a complementary manner. We envision that this novel method could be extended to synthesize other ternary oxides with hollow architectures for lithium-storage applications.

ASSOCIATED CONTENT

Supporting Information

Additional EDS, SEM and TEM micrographs of zinc−cobalt citrate microspheres with different aging time and BET of

double-shelled $ZnCo_2O_4$ hollow microspheres. This material is available free of charge via the Internet at http://pubs.acs.org/.

AUTHOR INFORMATION

Corresponding Author

*E-mail: dlpeng@xmu.edu.cn.

Notes

The authors declare no competing financial interest.

ACKNOWLEDGMENTS

The authors gratefully acknowledge financial support from the National Basic Research Program of China (2012CB933103), the National Outstanding Youth Science Foundation of China (Grant 50825101), and the National Natural Science Foundation of China (Grants 51171158 and 50971108).

REFERENCES

(1) Tarascon, J. M.; Armand, M. *Nature* **2001**, *414*, 359−367.
(2) Arico, A. S.; Bruce, P.; Scrosati, B.; Tarascon, J. M.; Schalkwijk, W. V. *Nat. Mater.* **2005**, *4*, 366−377.
(3) Cabana, J.; Monconduit, L.; Larcher, D.; Palacin, M. R. *Adv. Mater.* **2010**, *22*, E170−E192.
(4) Cherian, C. T.; Reddy, M. V.; Haur, S. C.; Chowdari, B. V. R. *RSC Adv.* **2013**, *3*, 3118−3123.
(5) Bruce, P. G.; Scrosati, B.; Tarascon, J. M. *Angew. Chem., Int. Ed.* **2008**, *47*, 2930−2946.
(6) Courtney, I. A.; Dahn, J. R. *J. Electrochem. Soc.* **1997**, *144*, 2045−2052.
(7) Sharma, Y.; Sharma, N.; Subba Rao, G. V.; Chowdari, B. V. R. *Chem. Mater.* **2008**, *20*, 6829−6839.
(8) Sharma, Y.; Sharma, N.; Subba Rao, G. V.; Chowdari, B. V. R. *J. Power Sources* **2009**, *192*, 627−635.
(9) Das, B.; Reddy, M. V.; Subba Rao, G. V.; Chowdari, B. V. R. *J. Mater. Chem.* **2011**, *21*, 1171−1180.
(10) Reddy, M. V.; Subba Rao, G. V.; Chowdari, B. V. R. *J. Mater. Chem.* **2011**, *21*, 10003−10011.
(11) Poizot, P.; Laruelle, S.; Grugeon, S.; Dupont, L.; Tarascon, J. M. *J. Power Sources* **2001**, *97*−*98*, 235−239.
(12) Badway, F.; Plitz, I.; Grugeon, S.; Laruelle, S.; Dolle, M.; Gozdz, A. S.; Tarascon, J. M. *Electrochem. Solid-State Lett.* **2002**, *5*, A115−A118.
(13) Sharma, Y.; Sharma, N.; Subba Rao, G. V.; Chowdari, B. V. R. *Adv. Funct. Mater.* **2007**, *17*, 2855−2861.
(14) Bavykin, D. V.; Friedrich, J. M.; Walsh, F. C. *Adv. Mater.* **2006**, *18*, 2807−2824.
(15) Taberna, L.; Mitra, S.; Poizot, P.; Simon, P.; Tarascon, J. M. *Nat. Mater.* **2006**, *5*, 567−573.
(16) Shi, Y. F.; Guo, B. K.; Corr, S. A.; Shi, Q. H.; Hu, Y. S.; Heier, K. R.; Chen, L. Q.; Seshadri, R.; Stucky, G. D. *Nano Lett.* **2009**, *9*, 4215−4220.
(17) Li, W. Y.; Xu, L. N.; Chen, J. *Adv. Funct. Mater.* **2005**, *15*, 851−857.
(18) Nam, K. T.; Kim, D. W.; Yoo, P. J.; Chiang, C. Y.; Meethong, N.; Hammond, P. T.; Chiang, Y. M.; Belcher, A. M. *Science* **2006**, *312*, 885−888.
(19) Poizot, P.; Laruelle, S.; Grugeon, S.; Dupont, L.; Tarascon, J. M. *Nature* **2000**, *407*, 496−499.
(20) Chen, J.; Xia, X. H.; Tu, J. P.; Xiong, Q. Q.; Yu, Y. X.; Wang, X. L.; Gu, C. D. *J. Mater. Chem.* **2012**, *22*, 15056−15061.
(21) Yang, X. L.; Fan, K. C.; Zhu, Y. H.; Shen, J. H.; Jiang, X.; Zhao, P.; Li, C. Z. *J. Mater. Chem.* **2012**, *22*, 17278−17283.
(22) Binotto, G.; Larcher, D.; Prakash, A. S.; Urbina, R. H.; Hegde, M. S.; Tarascon, J. M. *Chem. Mater.* **2007**, *19*, 3032−3040.
(23) Liu, J.; Xia, H.; Lu, L.; Xue, D. F. *J. Mater. Chem.* **2010**, *20*, 1506−1510.
(24) Reddy, M. V.; Zhang, B. C.; Loh, K. P.; Chowdari, B. V. R. *CrystEngComm* **2013**, *15*, 3568−3574.
(25) Reddy, M. V.; Zhang, B. C.; Li, J. E.; Nicholette; Zhang, K. M.; Chowdari, B. V. R. *Electrochem. Solid State Lett.* **2011**, *14*, A79−A82.
(26) Reddy, M. V.; Subba Rao,G. V.; Chowdari, B. V. R. *Chem. Rev.* April 2, 2013, DOI: 10.1021/cr3001884.
(27) Bruce, P. G.; Scrosati, B.; Tarascon, J. M. *Angew. Chem., Int. Ed.* **2008**, *47*, 2930−2946.
(28) Sharma, Y.; Sharma, N.; Rao, G. V. S.; Chowdari, B. V. R. *J. Power Sources* **2007**, *173*, 495−501.
(29) NuLi, Y. N.; Zhang, P.; Guo, Z. P.; Liu, H. K.; Yang, J. *Electrochem. Solid-State Lett* **2008**, *11*, A64−A67.
(30) Qiu, Y. C.; Yang, S. H.; Deng, H.; Jin, L. M.; Li, W. S. *J. Mater. Chem.* **2010**, *20*, 4439−4444.
(31) Alcántara, R.; Jaraba, M.; Lavela, P.; Tirado, J. L. *Chem. Mater.* **2002**, *14*, 2847−2848.
(32) Reddy, M. V.; Cai, Y.; Fan, J. H.; Loh, K. P.; Chowdari, B. V. R. *RSC Adv.* **2012**, *2*, 9619−9625.
(33) Sharma, Y.; Sharma, N.; Subba Rao, G. V.; Chowdari, B. V. R. *Solid State Ionics* **2008**, *179*, 587−597.
(34) Kim, H.; Seo, D. H.; Park, I.; Hong, J.; Park, K. Y.; Kang, K. *Chem. Mater.* **2012**, *24*, 720−725.
(35) Ai, C. C.; Yin, M. C.; Wang, C. W.; Sun, J. T. *J. Mater. Sci.* **2004**, *39*, 1077−1079.
(36) Reddy, M. V.; Kenrick, K. Y. H.; Tang, Y. W.; Chong, G. Y.; Leong, G. H.; Chowdari, B. V. R. *J. Electrochem. Soc.* **2011**, *158*, A1423−A1430.
(37) Liu, B.; Zhang, J.; Wang, X. F.; Chen, G.; Chen, D.; Zhou, C. W.; Shen, G. Z *Nano Lett.* **2012**, *12*, 3005−3011.
(38) Luo, W.; Hu, X. L.; Sun, Y. M.; Huang, Y. H. *J. Mater. Chem.* **2012**, *22*, 8916−8921.
(39) Tan, K. S.; Reddy, M. V.; Subba Rao, G. V.; Chowdari, B. V. R. *J. Power Sources* **2005**, *147*, 241−248.
(40) Reddy, M. V.; Subba Rao, G. V.; Chowdari, B. V. R. *J. Phys. Chem. C* **2007**, *111*, 11712−11720.
(41) Reddy, M. V.; Subba Rao, G. V.; Chowdari, B. V. R. *J. Power Sources* **2006**, *159*, 263−267.
(42) Zhao, X.; Reddy, M. V.; Liu, H.; Ramakrishna, S.; Subba Rao, G. V.; Chowdari, B. V. R. *RSC Adv.* **2012**, *2*, 7462−7469.
(43) Reddy, M. V.; Tung, B. D.; Yang, L.; Quang Minh, N. D.; Loh, K. P.; Chowdari, B. V. R. *J. Power Sources* **2013**, *225*, 374−381.
(44) Wang, X.; Wu, X. L.; Guo, Y. G.; Zhong, Y. T.; Cao, X. Q.; Ma, Y.; Yao, J. N. *Adv. Funct. Mater.* **2010**, *20*, 1680−1686.
(45) Xie, Q. S.; Li, J. G.; Tian, Q.; Shi, R. R. *J. Mater. Chem.* **2012**, *22*, 13541−13547.
(46) Cho, S.; Jang, J. W.; Jung, A.; Lee, S. H.; Lee, J.; Lee, J. S.; Lee, K. H. *Langmuir* **2011**, *27*, 371−378.
(47) Zhecheva, E.; Stoyanova, R.; Gorova, M.; Alcántara, R.; Morales, J.; Tirado, J. L. *Chem. Mater.* **1996**, *8*, 1429−1440.
(48) Che, P.; Fang, D.; Zhang, D.; Feng, J.; Wang, J.; Hu, N.; Meng, J. *J. Coord. Chem.* **2005**, *58*, 1581−1588.
(49) Milanova, M. M.; Arnaudov, M. G.; Getsova, M. M.; Todorovsky, D. S. *J. Alloys Compd.* **1998**, *264*, 95−103.
(50) Demadis, K. D.; Coucouvanis, D. *Inorg. Chem.* **1995**, *34*, 436−448.
(51) Dedryvère, R.; Laruelle, S.; Grugeon, S.; Poizot, P.; Gonbeau, D.; Tarascon, J. M. *Chem. Mater.* **2004**, *16*, 1056−1061.
(52) Barreca, D.; Massignan, C. *Chem. Mater.* **2001**, *13*, 588−593.
(53) Liu, J.; Xia, H.; Xue, D. F.; Lu, L. *J. Am. Chem. Soc.* **2009**, *131*, 12086−12087.
(54) Zeng, H. C. *J. Mater. Chem.* **2006**, *16*, 649−662.
(55) Liu, B.; Zeng, H. C. *Small* **2005**, *1*, 566−571.
(56) Duan, F.; Zhang, Q. H.; Wei, C. J.; Shi, D. J.; Chen, M. Q. *Mater. Lett.* **2013**, *92*, 231−234.
(57) Lai, X. Y.; Li, J.; Korgel, B. A.; Dong, Z. H.; Li, Z. M.; Su, F. B.; Du, J.; Wang, D. *Angew. Chem., Int. Ed.* **2011**, *50*, 2738−2741.
(58) Du, N.; Xu, Y. F.; Zhang, H.; Yu, J. X.; Zhai, C. X.; Yang, D. R. *Inorg. Chem.* **2011**, *50*, 3320−3324.
(59) Balaya, P.; Li, H.; Kienle, L.; Maier, J. *Adv.Funct.Mater.* **2003**, *13*, 621−625.

(60) Li, H.; Huang, X. J.; Chen, L. Q. *Electrochem. Solid State Lett.* **1998**, *1*, 241−243.
(61) Laruelle, S.; Grugeon, S.; Poizot, P.; Dolle, M.; Dupont, L.; Tarascon, J. M. *J. Electrochem. Soc.* **2002**, *149*, A627−A634.
(62) Zhou, L.; Wu, H. B.; Zhu, T.; Lou, X. W. *J. Mater. Chem.* **2012**, *22*, 827−829.